Supplementary Information For:

Molecularly imprinted layer-coated silica nanoparticle sensors with guest-induced fluorescence enhancement: Theoretical prediction and experimental observation

Jiawei Zhao ‡, Li Nie ‡, Liying Zhang, Yang Jin, Yan Peng, Shuhu Du * and Nan Jiang *

School of Pharmacy, Nanjing Medical University, Nanjing 210029, China

Table of contents

* Corresponding author. Tel.: +86 25 86868476; Fax: +86 25 86868476.
E-mail address: shuhudu@njmu.edu.cn; jiangnan@njmu.edu.cn
‡ These authors contributed equally.

1 DFT calculation

All calculations were performed with Gaussian 09 at B3LYP level with 6-31G(d,p) basis set.

1.1 Conformation search of monomers

The conformational diversities of three functional monomers could be easily seen from the nearly degenerate energies of various configurations. Two dihedral angles (ω_1 and ω_2, as shown in Table S1) of monomers were employed to scan their potential energy surface (PES) by means of restrained geometric optimization (Fig. S1). As illustrated in Table S1, three minima of 2-AAQ with ω_1 (ω_2) of 180.0° (–180.0°), 156.2° (–13.6°) and 0.0° (0.0°) for trans-trans, trans-cis and cis-cis conformations were found, respectively. Four minima of 3-AAQ with ω_1 (ω_2) of 180.0° (–180.0°), 0.0° (–180.0°), 147.1° (–7.1°) and 42.7° (6.8°) for tran-trans, cis-trans, trans-cis and (+)gauche-cis conformers were located, respectively. And three minima of 8-AAQ were located, with ω_1 (ω_2) of 180.0° (180.0°), 159.9° (14.9°) and –49.5° (–4.8°) for the trans-trans, trans-cis and (–)gauche-cis, respectively. Detail informations of monomers were listed in Table S1-S4.

Table S1. Geometric and energetic informations of various conformations of 2-AAQ, 3-AAQ and 8-AAQ.

Monomer			Conformation	ω_1 (°)	ω_2 (°)	ΔE (kcal mol^{-1})
2-AAQ				*a*→*b*→*c*→*d*	*b*→*c*→*e*→*f*	
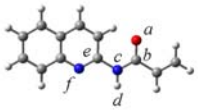	*a*: O	*b*: C	trans-trans	180.0	–180.0	0.00
	c: N	*d*: H	cis-cis	0.0	0.0	4.33
	e: C	*f*: N	trans-cis	156.2	13.6	6.15
3-AAQ				*a*→*b*→*c*→*d*	*b*→*c*→*e*→*f*	
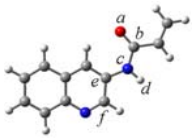	*a*: O	*b*: C	trans-trans	180.0	180.0	0.00
	c: N	*e*: C	cis-trans	0.0	180.0	1.69
	d: H	*f*: C	trans-cis	147.1	7.1	4.46
			(+)gauche-cis	42.7	6.8	4.71
8-AAQ				*a*→*b*→*c*→*d*	*b*→*c*→*e*→*f*	
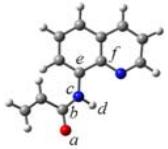	*a*: O	*b*: C	trans-trans	180.0	180.0	0.00
	c: N	*d*: H	trans-cis	159.9	14.9	6.59
	e: C	*f*: C	(–)gauche-cis	–49.5	–4.8	11.11

Table S2. The electronic structural parameters of 2-AAQ calculated at the B3LYP/6-31G(d,p) level in gas phase.

		Conformation		
		trans-trans	cis-cis	trans-cis
		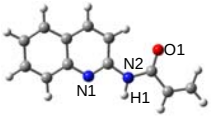	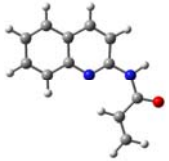	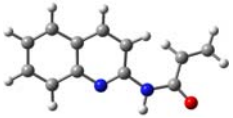
NBO charge	N1	–0.49	–0.48	–0.48
	N2	–0.63	–0.64	–0.64
	H1	0.44	0.45	0.45
	O1	–0.62	–0.64	–0.64
Frequency (cm^{-1})	ν_{N3-H5}	3465	3453	3462
Dipole moment (debye)	$\lvert\vec{\mu}\rvert$	1.40	4.21	3.74

Table S3. The electronic structural parameters of 3-AAQ calculated at the B3LYP/6-31G(d,p) level in gas phase.

		Conformation			
		trans-trans	cis-trans	trans-cis	(+)gauche-cis
		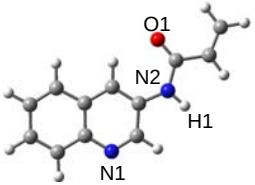	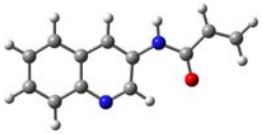	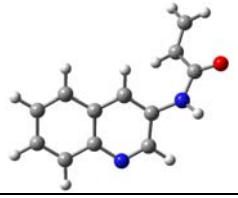	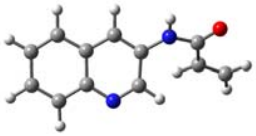
NBO charge	N1	–0.42	–0.43	–0.43	–0.42
	N2	–0.65	–0.62	–0.62	–0.66
	H1	0.43	0.42	0.42	0.44
	O1	–0.60	–0.61	–0.62	–0.61
Frequency (cm^{-1})	ν_{N3-H5}	3449	3471	3475	3454
Dipole moment (debye)	$\lvert\vec{\mu}\rvert$	3.03	5.04	2.30	3.06

Table S4. The electronic structural parameters of 8-AAQ calculated at the B3LYP/6-31G(d,p) level in gas phase.

		Conformation		
		trans-trans	trans-cis	(−)gauche-cis
		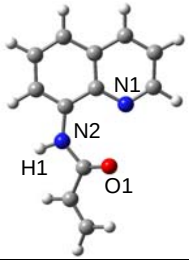	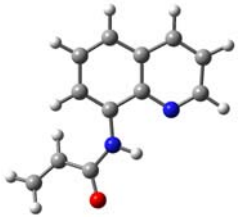	
NBO charge	N1	−0.48	−0.47	−0.44
	N2	−0.62	−0.63	−0.65
	H1	0.45	0.46	0.44
	O1	−0.62	−0.60	−0.61
Frequency (cm^{-1})	ν_{N3-H5}	3401	3407	3604
Dipole moment (debye)	$\lvert\vec{\mu}\rvert$	3.41	4.70	5.20

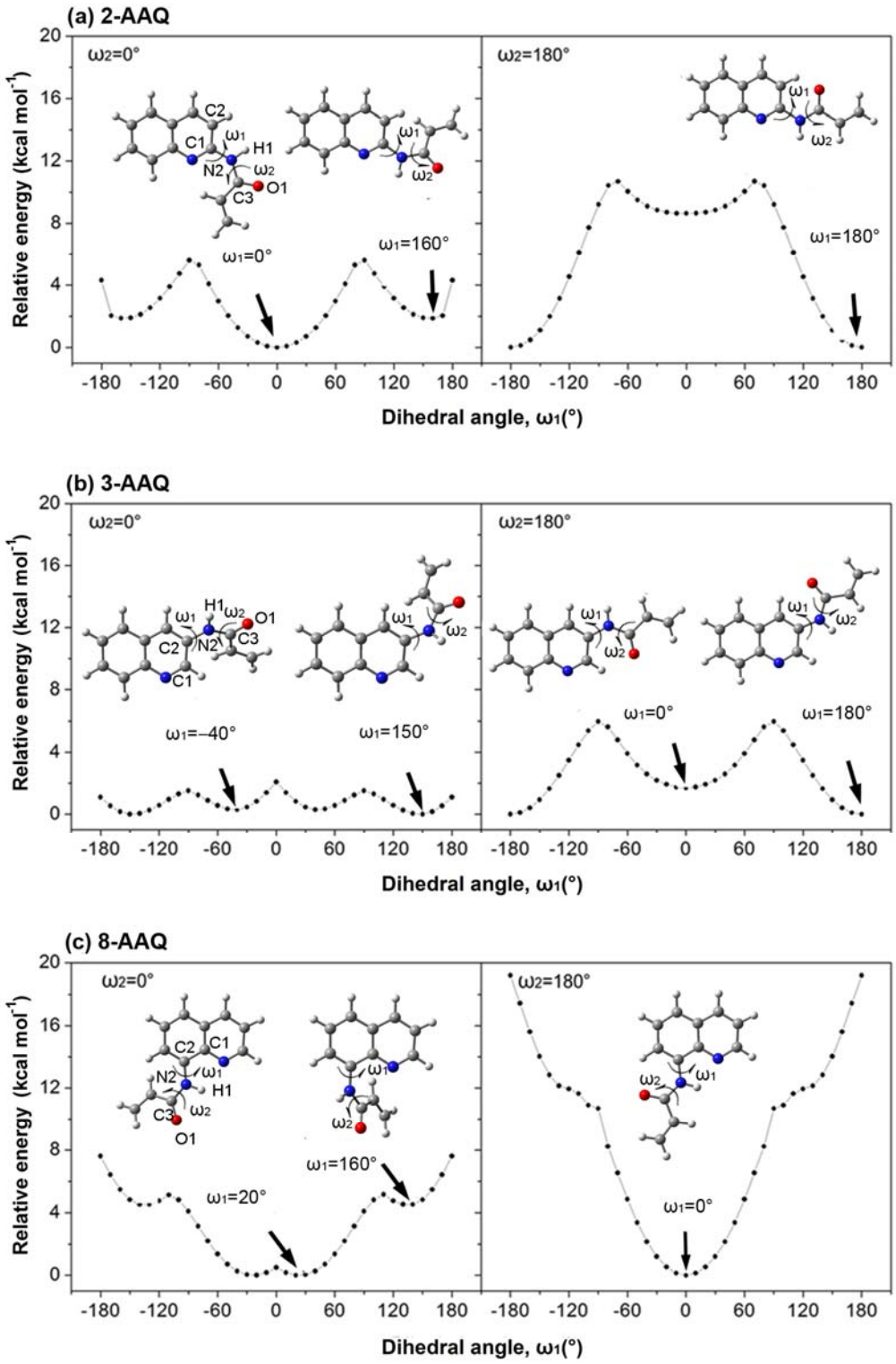

Fig. S1 Potential energy curves and local minima of 2-AAQ, 3-AAQ and 8-AAQ.

1.2 Construction of monomer-template complexes

Table S5. Interaction energies of 2-AAQ···MA, 3-AAQ···MA and 8-AAQ···MA complexes at B3LYP/6–31G(d,p) level in gas phase, respectively.

Complex	Interaction energy[a] (kcal mol^{-1})							
	I	II	III	IV	V	VI	VII	E_{Total}^{ave}
2-AAQ···MA	–17.98 (–15.11)	–14.23 (–11.90)	–12.81 (–8.87)	–8.00 (–6.08)	–7.65 (–5.66)	–7.20 (–5.43)	–7.10 (–4.61)	–10.71 (–8.23)
3-AAQ···MA	–14.75 (–12.44)	–14.23 (–12.88)	–12.81 (–5.62)	–8.00 (–5.11)	–7.65 (–5.42)	–7.20 (–5.94)	–7.10 (–5.58)	–10.25 (–7.57)
8-AAQ···MA	–15.24 (–12.64)	–12.90 (–12.96)	–7.47 (–5.76)	–7.86 (–5.97)	–7.86 (–5.82)	–7.50 (–5.64)	–7.34 (–5.31)	–8.33 (–7.70)

[a] The BSSE corrected interaction energies are given in the parentheses.

Table S6. The geometric parameters and interaction energies of 2-AAQ···MA, 3-AAQ···MA and 8-AAQ···MA complexes in gas phase, respectively.

Ratio	Complex	$r^{ave}_{H\cdots N(O)}$ (Å)	$\angle^{ave}_{N-H\cdots N(O)}$ (°)	E^{H-bond}_{Total} (kcal mol^{-1})	E_{Total} [a] (kcal mol^{-1})	E^{ave}_{Total} (kcal mol^{-1})	E_{elec} [b] (kcal mol^{-1})	E^{SP}_{elec} [c] (kcal mol^{-1})
1 : 1	2-AAQ···MAI	1.96	173.3	–15.23	–17.98(–15.11)	–15.11	–420.72	–139.33
	2-AAQ···MAII	1.98	176.5	–8.25	–14.23(–11.90)	–10.39	--	--
	2-AAQ···MAIII	2.04	176.0	–8.87	–12.81(–8.87)		--	--
	3-AAQ···MAI	1.92	176.6	–12.96	–14.75(–12.44)	–12.66	--	--
	3-AAQ···MAII	1.92	176.7	–12.65	–14.23(–12.88)		--	--
	8-AAQ···MAI	1.99	169.9	–11.54	–12.90(–12.96)	–12.80	--	--
	8-AAQ···MAII	1.92	177.2	–12.64	–15.24(–12.64)		--	--
2 : 1	$(2\text{-AAQ})_2$···MAI	1.92	174.0	–30.85	–35.38(–29.87)	–29.87	–460.04	–276.62
	$(2\text{-AAQ})_2$···MAII	1.97	176.5	–17.19	–28.34(–23.29)	–21.83	--	--
	$(2\text{-AAQ})_2$···MAIII	2.03	176.7	–18.09	–25.40(–20.36)		--	--
	$(3\text{-AAQ})_2$···MAI	1.91	176.6	–21.24	–30.60 (–25.42)	–24.90	--	--
	$(3\text{-AAQ})_2$···MAII	1.92	177.1	–20.85	–29.17(–24.37)		--	--
	$(8\text{-AAQ})_2$···MAI	2.00	169.7	–23.66	–25.32(–25.76)	–25.56	--	--
	$(8\text{-AAQ})_2$···MAII	1.91	176.9	–21.46	–30.58(–25.36)		--	--
3 : 1	$(2\text{-AAQ})_3$···MAI	1.97	173.3	–46.84	–68.34(–44.08)	–44.08	–465.03	–416.23
	$(8\text{-AAQ})_3$···MAI	2.00	169.8	–36.85	–37.43(–38.46)	–38.46	--	--
4 : 1	$(2\text{-AAQ})_4$···MAI	1.97	173.3	–42.92	–53.55(–41.69)	–41.69	–525.28	–407.26

[a] The BSSE corrected interaction energies are given in the parentheses.

[b] Electrostatic energies are calculated through molecule dynamic method.

[c] Electrostatic energies between point charges are calculated through classic function.

Table S7. N–H stretching frequency of the monomers, $(2\text{-AAQ})_n\cdots$MA, $(3\text{-AAQ})_n\cdots$MA and $(8\text{-AAQ})_n\cdots$MA complexes (n=1, 2, 3 and 4) optimized at B3LYP/6-31G(d,p) level, respectively.

Monomer/Complex	Conformation	Mode	Frequency(cm^{-1})
2-AAQ			
	trans-cis	ν_0 (N2–H1)	3462
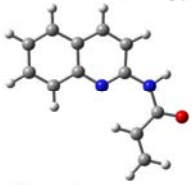	cis-cis	ν_0 (N2–H1)	3453
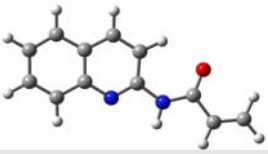	trans-trans	ν_0 (N2–H1)	3465
3-AAQ			
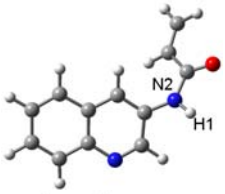	trans-cis	ν_0 (N2–H1)	3475
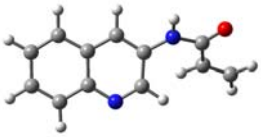	(+)gauche-cis	ν_0 (N2–H1)	3454
8-AAQ			
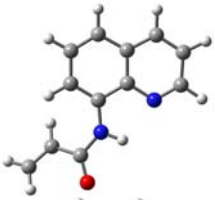	trans-cis	ν_0 (N2–H1)	3407
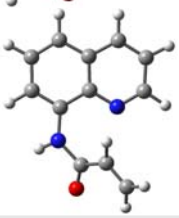	(−)gauche-cis	ν_0 (N2–H1)	3604
Melamine			
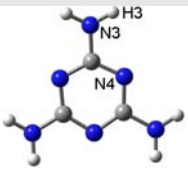	MA	ν_0^s (N3–H3)	3625
		ν_0^{as} (N3–H3)	3764

2-AAQ···MA complex			
	I	ν (N2–H1)	2883
		ν^s (N3–H3)	3305
		ν^s (N5–H4)	3320
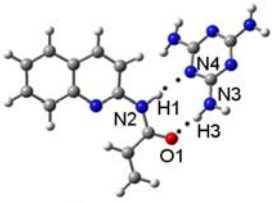	II	ν (N2–H1)	3177
		ν^s (N3–H3)	3274
	III	ν (N2–H1)	3180
		ν^s (N3–H3)	3239
3-AAQ···MA complex			
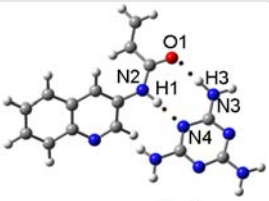	I	ν (N2–H1)	3026
		ν^s (N3–H3)	3285
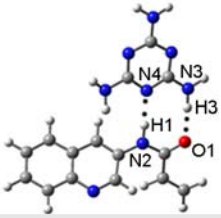	II	ν (N2–H1)	3040
		ν^s (N3–H3)	3272
8-AAQ···MA complex			
	I	ν (N2–H1)	3046
		ν^s (N3–H3)	3279
		ν^s (N5–H4)	3361
	II	ν (N2–H1)	3063
		ν^s (N3–H3)	3249

$(2\text{-AAQ})_2\cdots$MA complex			
	I	ν (N2–H1)	2912
		ν^{s} (N3–H3)	3315
		ν^{s} (N5–H4)	3325
		ν^{as} (N3–H5)	3413
		ν (N10–H9)	2872
		ν^{s} (N7–H7)	3289
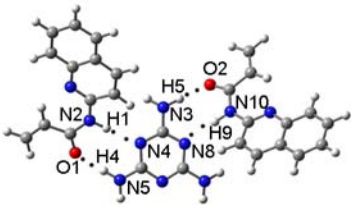	II	ν (N2–H1)	3188
		ν^{s} (N5–H4)	3261
		ν^{as} (N3–H5)	3249
		ν (N10–H9)	3167
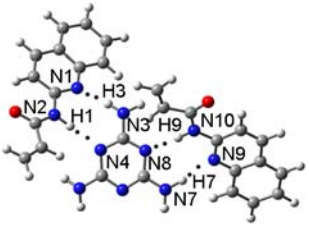	III	ν (N2–H1)	3186
		ν^{s} (N3–H3)	3228
		ν^{s} (N7–H7)	3211
		ν (N10–H9)	3192
$(3\text{-AAQ})_2\cdots$MA complex			
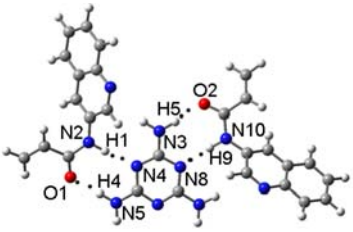	I	ν (N2–H1)	3053
		ν^{s} (N5–H4)	3275
		ν^{as} (N3–H5)	3267
		ν (N10–H9)	3030
	II	ν (N2–H1)	3060
		ν^{s} (N5–H4)	3263
		ν^{as} (N3–H5)	3252
		ν (N10–H9)	3037

$(8\text{-AAQ})_2\cdots$MA complex			
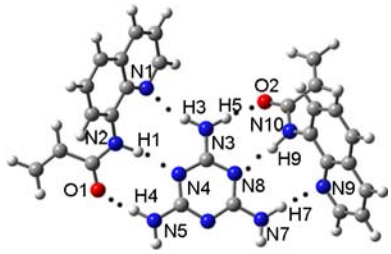	I	ν (N2–H1)	3060
		ν^{s} (N3–H3)	3294
		ν^{s} (N5–H4)	3276
		ν^{as} (N3–H5)	3452
		ν (N10–H9)	3013
		ν^{s} (N7–H7)	3374
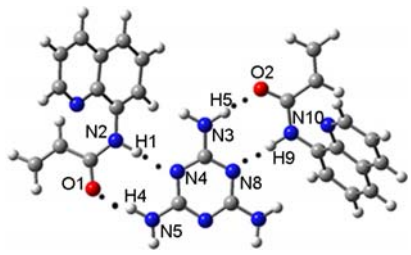	II	ν (N2–H1)	3069
		ν^{s} (N5–H4)	3239
		ν^{as} (N3–H5)	3251
		ν (N10–H9)	3050
$(2\text{-AAQ})_3\cdots$MA complex			
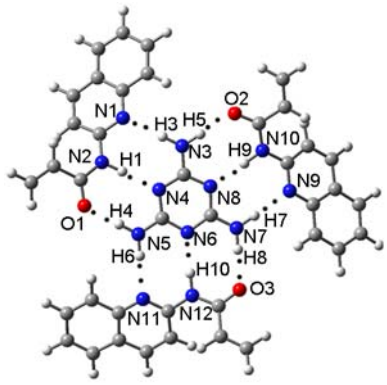	I	ν (N2–H1)	2924
		ν^{s} (N3–H3)	3315
		ν^{s} (N5–H4)	3292
		ν^{as} (N3–H5)	3423
		ν (N10–H9)	2896
		ν^{s} (N7–H7)	3292
		ν (N12–H10)	2892
		ν^{as} (N5–H6)	3423
		ν^{as} (N7–H8)	3417

$(8\text{-AAQ})_3\cdots$MA complex			
	I	ν (N2–H1)	3051
		ν^{s} (N3–H3)	3300
		ν^{s} (N5–H4)	3284
		ν^{as} (N3–H5)	3458
		ν (N10–H9)	3032
		ν^{s} (N7–H7)	3284
		ν (N12–H10)	3030
		ν^{as} (N5–H6)	3457
		ν^{as} (N7–H8)	3455
$(2\text{-AAQ})_4\cdots$MA complex			
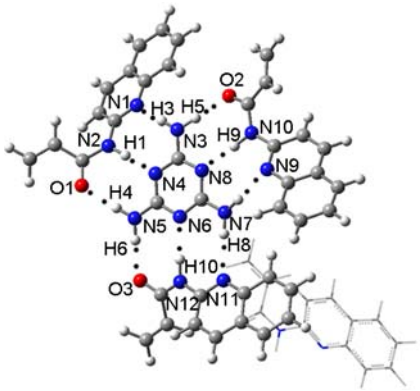	I	ν (N2–H1)	3028
		ν^{s} (N3–H3)	3319
		ν^{s} (N5–H4)	3300
		ν^{as} (N3–H5)	3449
		ν (N10–H9)	2953
		ν^{s} (N7–H7)	3288
		ν (N12–H10)	2914
		ν^{as} (N5–H6)	3420
		ν^{as} (N7–H8)	3408

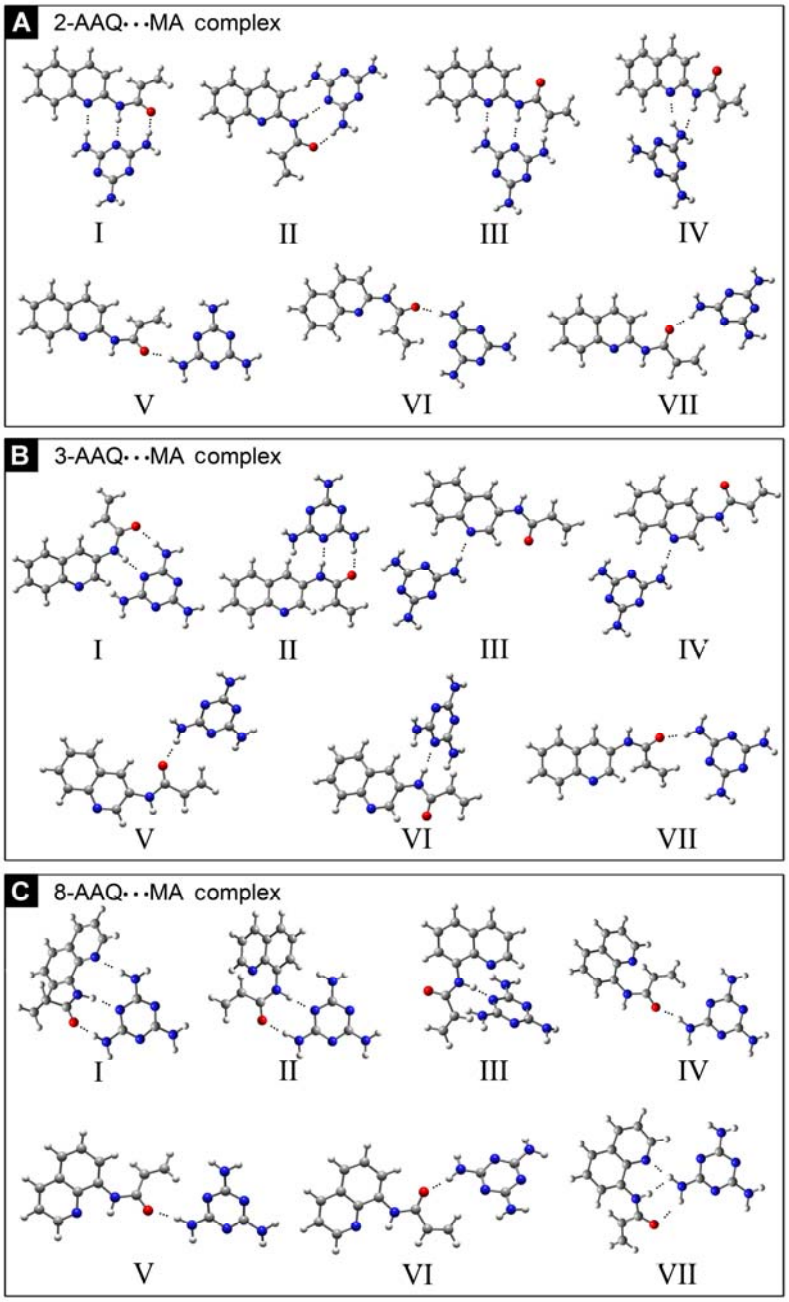

Fig. S2 The optimized geometries of (A) 2-AAQ···MA complex, (B) 3-AAQ···MA complex and (C) 8-AAQ···MA complex at the B3LYP/6-31G(d,p) level.

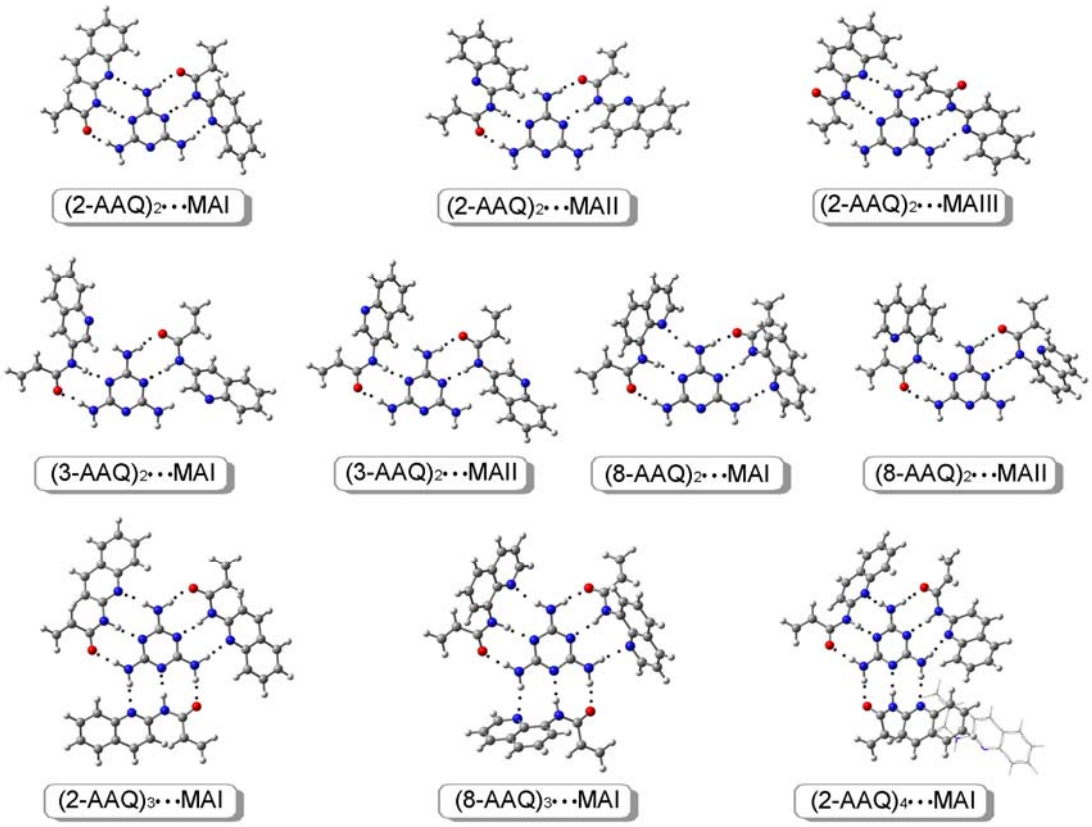

Fig.e S3. Conformations of (2-AAQ)$_n$···MA, (3-AAQ)$_n$···MA and (8-AAQ)$_n$···MA complexes (n = 2, 3 and 4).

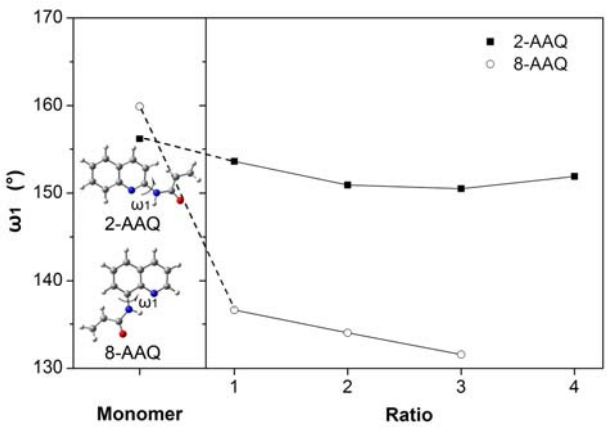

Fig. S4 The evolution of ω_1 of monomer with the change of molar ratio of monomer to template.

1.3 Electrostatic interaction between 2-AAQ and MA

The NBO atomic charges on the nitrogen and hydrogen atoms (Table S8) suggest that these strong hydrogen bonds are very polar and a substantial electrostatic interaction was present. The electrostatic energy, E_{elec} (kcal mol^{-1}), of the present monomer-template systems is evaluated by the classical Coulomb potential:

$$E_{elec} = 330.26 \times \frac{q_i q_j}{r_{ij}} \quad (1)$$

where q_i and q_j is the partial charges centered on atoms i and j, respectively. And r_{ij} is the distance between atoms i and j.

As plotted in Fig. S5, the electrostatic interaction was individually strengthened as the molar ratio of monomer to template increased from 1 : 1 to 3 : 1. Surprisingly, when the molar ratio was up to 4 : 1, the electrostatic interactions were somewhat decreased, along with the lengthened hydrogen bonding distances, which could be due to the influence of intermolecular steric effect. The steric effect was evaluated by Van der Waals energy. With the increment of functional monomers, the Van der Waals force of complexes increased gradually. In the range from 1 : 1 to 3 : 1, the electrostatic attraction was dominant, leading to the strong intermolecular interactions. However, when the ratio was up to 4 : 1, the steric repulsion was obvious, resulting in the weak intermolecular interactions.

Table S8. The interatomic distances and atomic charges of (2-AAQ)$_n$···MA complexes (n=1, 2, 3 and 4) optimized at B3LYP/6-31G(d,p) level.

Ratio	Complex	Interatomic distance (Å)		Atom	Charge
1 : 1		r_{H1-N4}	1.87	N1	–0.51
				H1	0.47
		r_{H3-N1}	2.09	H3	0.44
				H4	0.44
		r_{H4-O1}	1.93	O1	–0.63
				N4	–0.68
2 : 1		r_{H3-N1}	2.09	N1	–0.50
				H1	0.47
		r_{H1-N4}	1.90	O1	–0.64
				O2	–0.64
		r_{H4-O1}	1.92	N4	–0.68
				H3	0.43
		r_{H9-N8}	1.89	H4	0.44
				H5	0.44
		r_{H7-N9}	2.07	H7	0.43
				H9	0.47
		r_{H5-O2}	1.92	N8	–0.69
				N9	–0.50
3 : 1	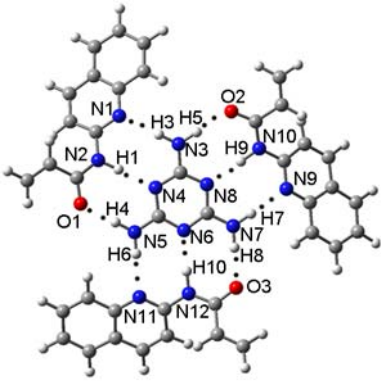	r_{H3-N1}	2.07	N1	–0.50
				H1	0.47
		r_{H1-N4}	1.92	O1	–0.64
				O2	–0.64
		r_{H4-O1}	1.92	O3	–0.64
				N4	–0.69
		r_{H9-N8}	1.92	H3	0.43
				H4	0.44
		r_{H7-N9}	2.06	H5	0.44
				N6	–0.69

		r_{H5-O2}	1.91	H6	0.43
				H7	0.43
		r_{H6-N11}	2.07	H8	0.44
				N8	–0.69
		r_{H10-N6}	1.92	H9	0.47
				N9	–0.50
		r_{H8-O3}	1.91	H10	0.47
				N11	–0.50
4 : 1	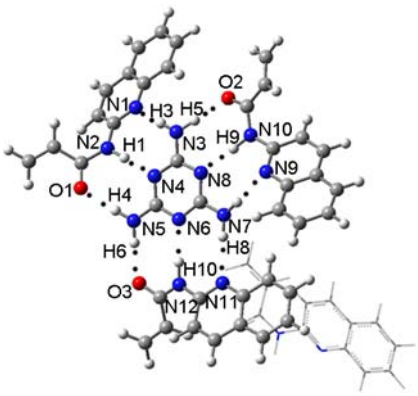	r_{H3-N1}	2.06	N1	–0.50
				H1	0.47
		r_{H1-N4}	1.91	O1	–0.63
				O2	–0.64
		r_{H4-O1}	1.95	O3	–0.63
				N4	–0.68
		r_{H9-N8}	1.97	H3	0.43
				H4	0.44
		r_{H7-N9}	2.22	H5	0.43
				N6	–0.69
		r_{H5-O2}	1.89	H6	0.44
				H7	0.43
		r_{H6-N11}	2.15	H8	0.43
				N8	–0.69
		r_{H10-N6}	2.00	H9	0.47
				N9	–0.50
		r_{H8-O3}	1.89	H10	0.47
				N11	–0.51

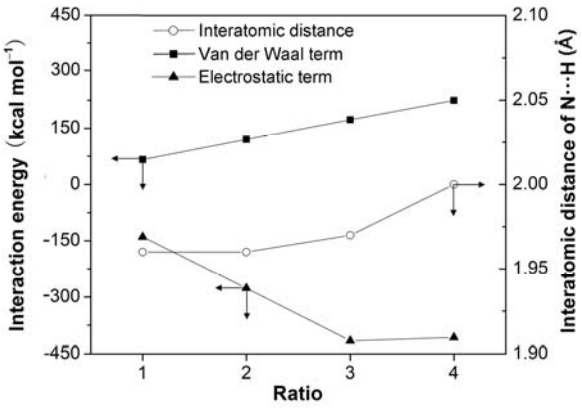

Fig. S5 Evolution of Van der Waals, electrostatic interaction and interatomic distance with the change of ratio of 2-AAQ to MA, respectively.

1.4 π-π stacking interaction between 2-AAQ and MA

The π-π stacking interaction between 2-AAQ and MA was investigated through DFT method. As shown in Fig S16, the parallel ring planes in the initial MA···2-AAQ configuration were twisted after optimization. In addition, the interaction energy was only 9.97 kcal mol^{-1}, much lower than the interaction energy (about 14−18 kcal mol^{-1}) in the complexes formed by H-bonding. So, this result revealed that the π-π stacking could be negligible in the complex of MA and 2-AAQ.

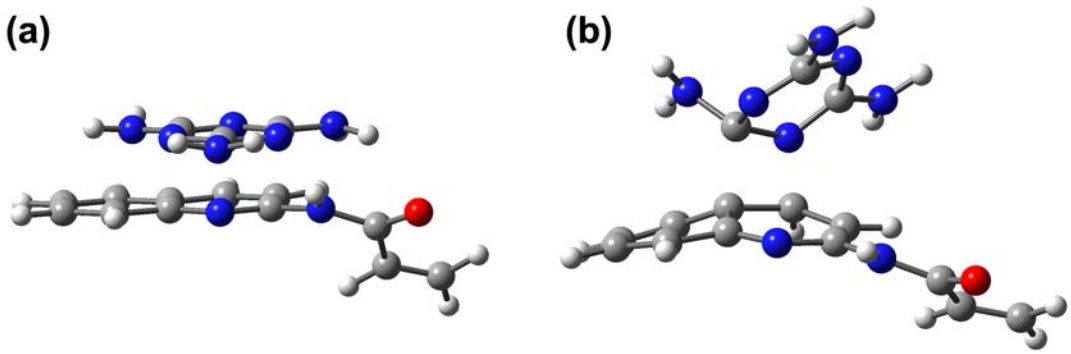

Fig. S16 The initial and optimized configurations of 2-AAQ···MA complex formed by π-π stacking: (a) Initial configuration; (b) Optimized configuration.

2. Experiment

2.1 Synthesis of 2-AAQ monomer

To synthesize 2-formatequinoline, 20.0 mmol of 2-carboxylquinoline (**1**) was first dissolved in 40 mL of ethanol. Then, 40.0 mmol of thionyl chloride was dropwised into the above solution while cooled in ice bath. The mixture was refluxed for 4 h under agitation. After the reaction had completed, the mixture was filtrated to remove the excess impurity and dried. Thus, the precursor, 2-formatequinoline (**2**), was obtained.

Compound **2** (18.4 mmol) was dissolved in 30 mL of hydrazine hydrate. The mixture was refluxed for 6 h. After the completion of the reaction, the reaction mixture was cooled to room temperature. The precipitated product was collected by filtration, washed with cold water and dried under vacuum. So, the intermediate, 2-acylhydrazinequinoline (**3**), was obtained.

Compound **3** (16.7 mmol) was dissolved in 30 mL of 2 M hydrochloric acid solution, then the mixture of sodium nitrite (20.0 mmol) in 7 mL of water was added into the above solution, stirred under low temperature (0-5 °C) for 0.5 h and adjusted pH to 7.0 with saturated sodium carbonate solution. The precipitated solid was filtered and re-dissolved in 30 mL of glacial acetic acid. The mixture was refluxed for 4 h, distillated to remove the solvent and then the residues were separated by silica column chromatography. Therefore, the intermediate, 2-aminoquinoline (**4**), was obtained.

Compound **4** (10.8 mmol) and triethylamine (17.2 mmol) were first dissolved in 30 mL of dichloromethane. Then, acryloyl chloride (13.0 mmol) was slowly added into the above solution under ice bath and reacted overnight at room temperature. The reaction solution (organic phase) was partitioned three times with equal volume of saturated soduim chloride solution (water phase). The water phase (upper layer) was removed. Subsequently, the organic phase (lower layer) was evaporated to dryness under vacuum. The residues were separated by silica column chromatography. Finally, the fluorescent monomer, 2-acrylamidoquinoline

(2-AAQ) was obtained and reserved in the fridge. The synthesis route is shown as Fig. S6.

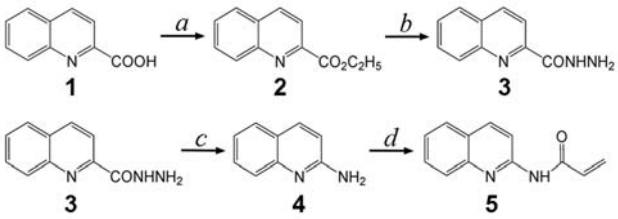

Fig. S6 Synthetic route of 2-AAQ.

2.2 Structural identification of 2-AAQ monomer

Identification of 2-AAQ was confirmed by MS, UV, IR and NMR (Fig. S7-S11). Molecular formula of 2-AAQ was established as $C_{12}H_{10}N_2O$ on the basis of positive-mode HRMS (*m/z* 221.0632, $[M+Na]^+$). Its UV spectrum showed the existence of phenyl group based on the absorption at 257 nm and pyridine ring group based on the absorptions at 318 nm and 332 nm. The IR absorption bands indicated the presence of secondary amino group (3230 cm^{-1}) and amide group (1670 cm^{-1}). In the ^1H NMR spectrum, six proton signals of quinoline ring resonated at 7.445-7.477 (m, 1H), 7.654-7.687 (m, 1H), 7.785-7.832 (m, 2H), 8.189-8.207 (d, 1H), 8.497-8.515 (d, 1H); one proton signal of amide group resonated at 8.506 (s, 1H) and three proton signals of alkene group resonated at 5.831-5.854(dd, 1H), 6.284-6.339(dd, 1H), 6.497-6.532(dd, 1H). The ^{13}C NMR spectrum displayed 12 carbon signals corresponding to nine carbons in the quinoline ring, one carbon in the carbonyl group and two carbons participating in double bond. Therefore, from these structural elements the formation of 2-AAQ could be identified.

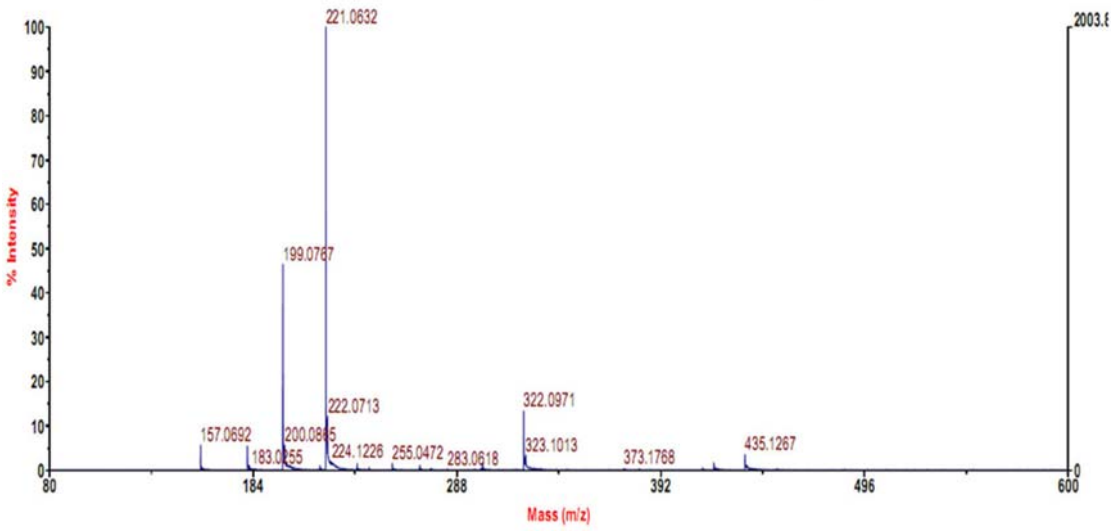

Fig. S7 HRMS spectrogram for 2-AAQ.

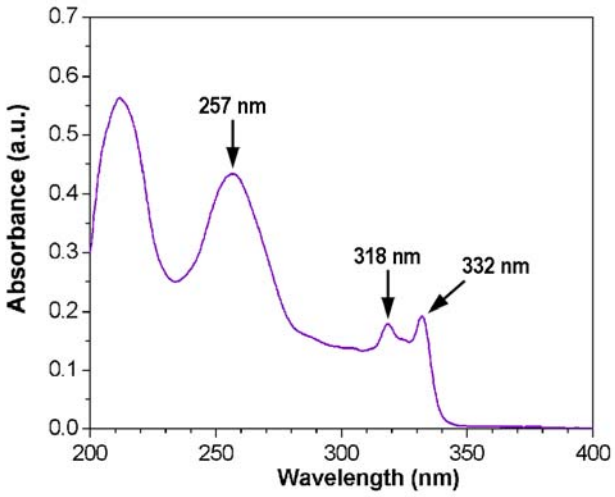

Fig. S8 UV spectrogram for 2-AAQ.

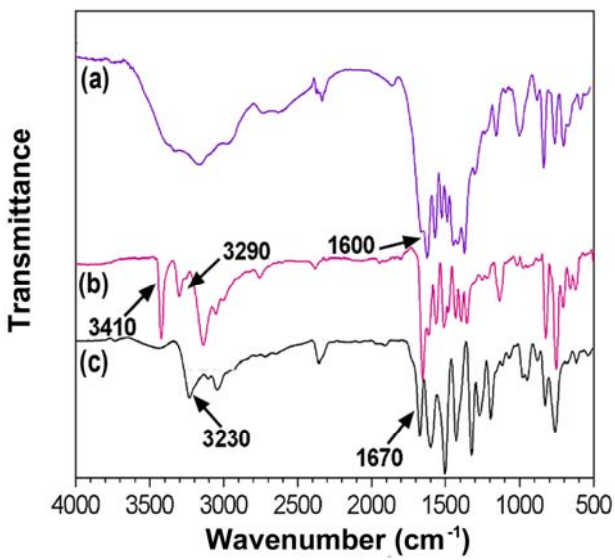

Fig. S9 FT-IR spectra of (a) acryloyl chloride, (b) 2-AQ and (c) 2-AAQ.

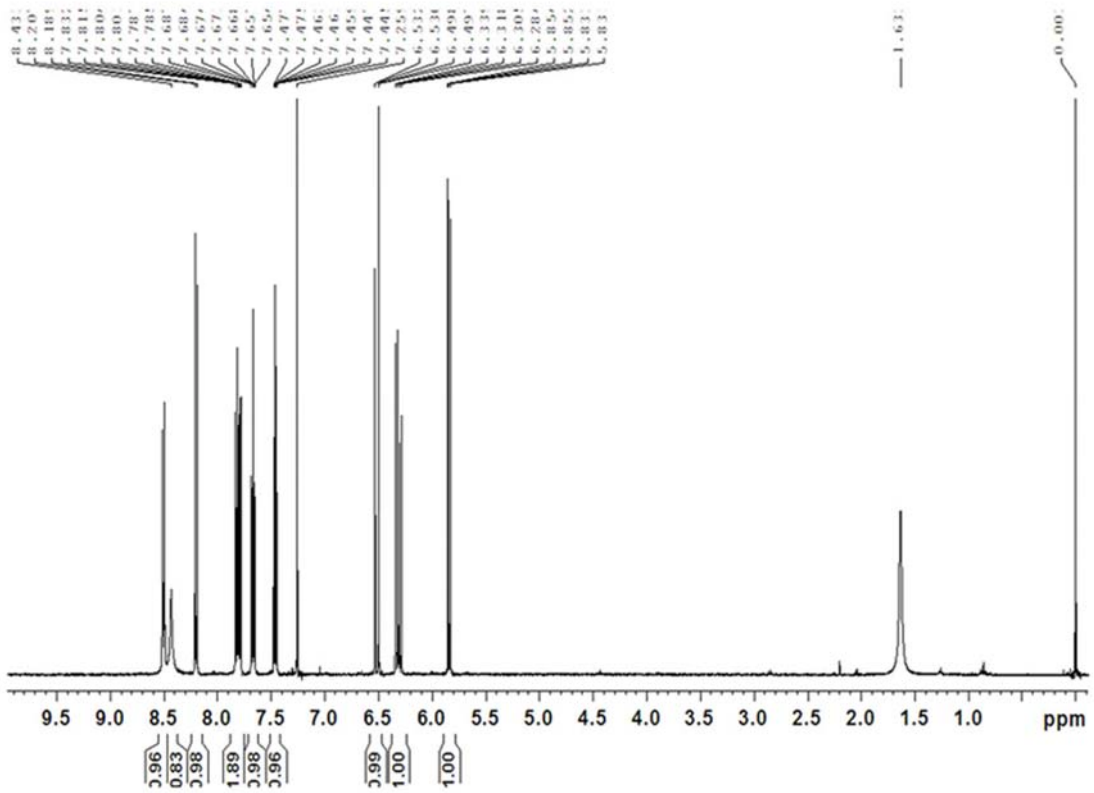

Fig. S10 ^{1}H NMR spectrogram for 2-AAQ (300 MH_z, $CDCl_3$).

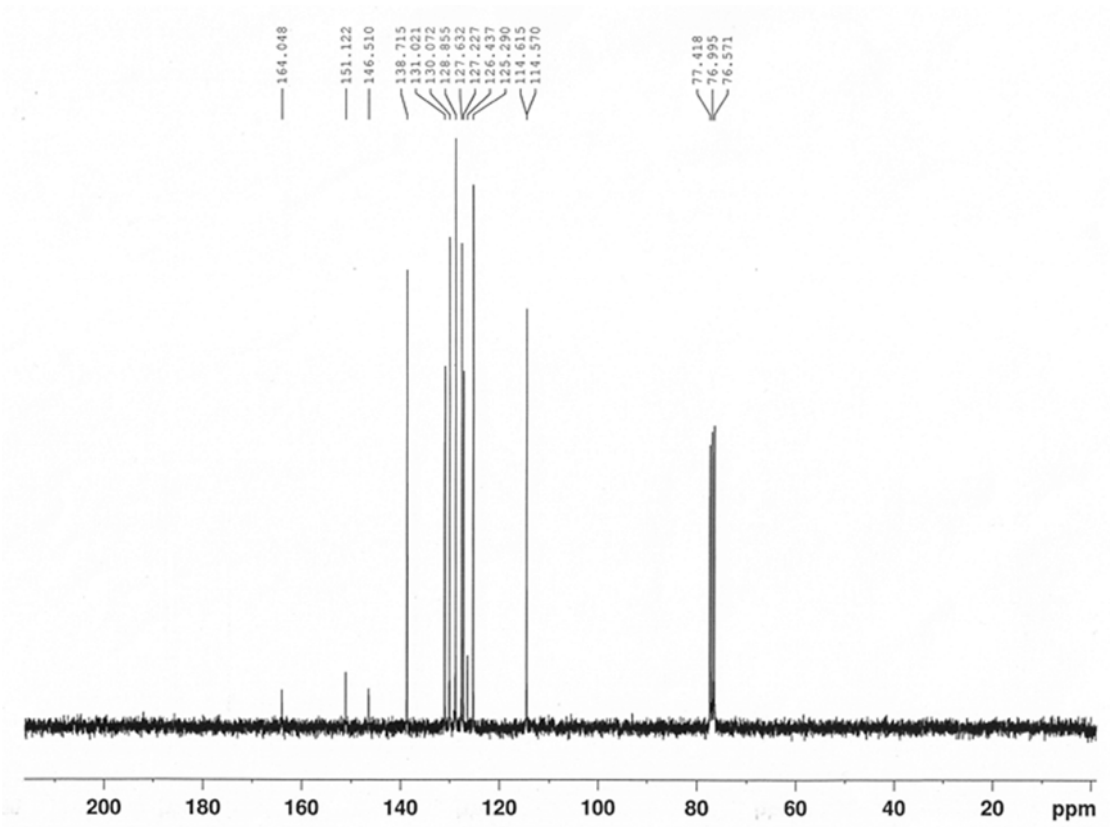

Fig. S11 ^{13}C NMR spectrogram for 2-AAQ (300 MH_z, $CDCl_3$).

2.3 Preparation of MA-imprinted nanoparticles

Typically, MPTS-silica nanoparticles (100 mg) were dispersed in 50.0 mL of DMSO by ultrasonication, then MA (0.024 mmol), 2-AAQ (0.076 mmol), EGDMA (0.480 mmol) and AIBN (10 mg) were added into the above solution. The mixed solution was purged with high-purity nitrogen for 10 min while cooled in ice bath. A three-step temperature polymerization reaction was carried out in an incubating shaker with a rate of 300 rpm. The polymerization was first done at 50 °C for 6 h, and then maintained at 60 °C for 24 h. Subsequently, the temperature was raised from 60 to 75 °C in 1 h with the rate of 0.25 °C min $^{-1}$ and the products were further aged at 75 °C for 6 h to obtain high cross-linking density. The resulting nanoparticles were separated from the mixed solution by centrifugation, rinsed in sequence with DMSO and methanol, cleaned by methanol/acetic acid (9 : 1, v/v) and dried under vacuum. The resultant SiO_2@MA-MIP nanoparticles were obtained (Fig. S12).

The non-imprinted nanoparticles (SiO_2@NIP) were also prepared using an identical procedure but without the addition of template.

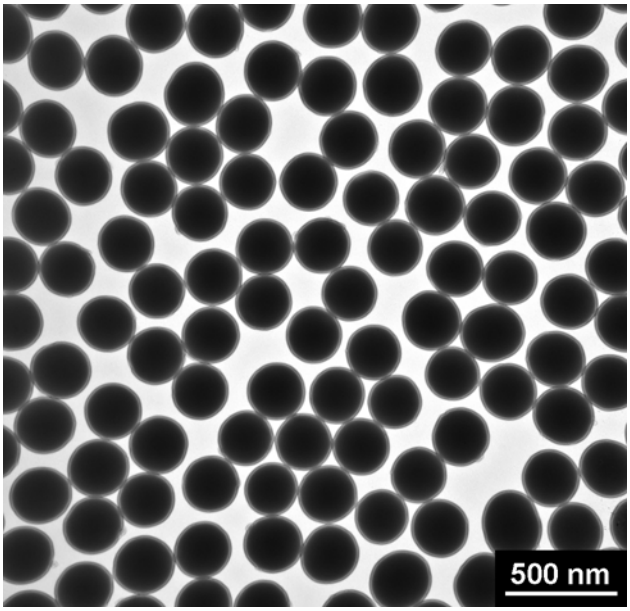

Fig. S12 TEM image of SiO_2@MA-MIP nanoparticles.

2.4 Binding performance

Two hundred milligrams of SiO_2@MA-MIP/SiO_2@NIP nanoparticles were suspended in 2.0 mL of methanol with a series of standard solutions, respectively. After incubation under a reciprocating shaking-table at room temperature for 40 min, the nanoparticles in the solution were removed through a 0.22 μm microporous membrane after reaching adsorption equilibrium and the equilibrium concentration of SiO_2@MA-MIP/SiO_2@NIP nanoparticles was determined by HPLC (Fig. S13). The binding amount of MA was calculated by the difference between the total amount and the residual amount in solution. Meanwhile, the binding kinetics was tested by monitoring the temporal evolution of MA concentration in the solutions.

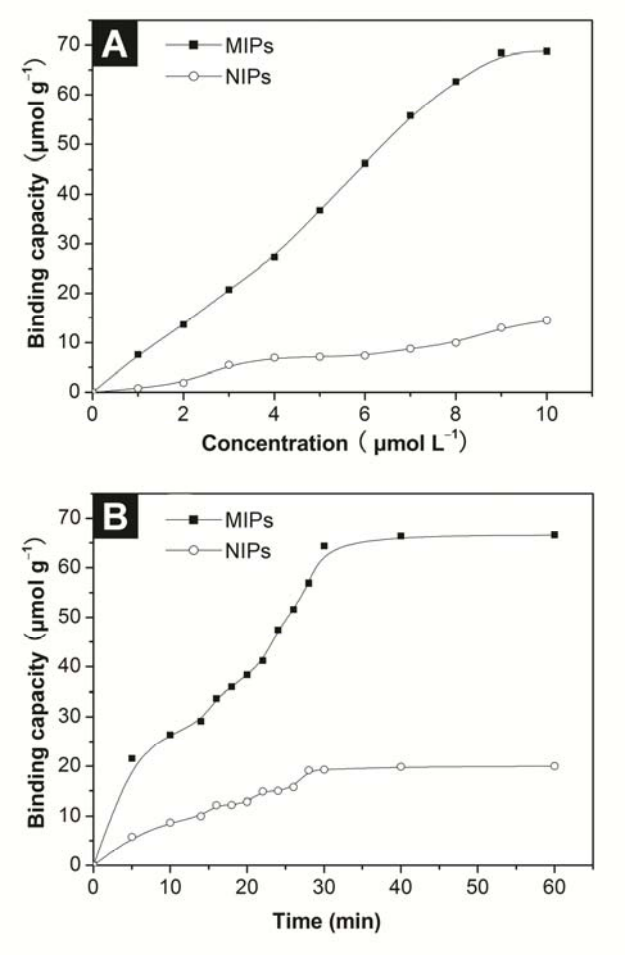

Fig. S13 (A) Rebinding capacity curves of SiO_2@MA-MIP and SiO_2@NIP to MA. (B) Adsorption time curves of SiO_2@MA-MIP and SiO_2@NIP to MA.

2.5 Investigation of fluorescent effect from pure 2-AAQ

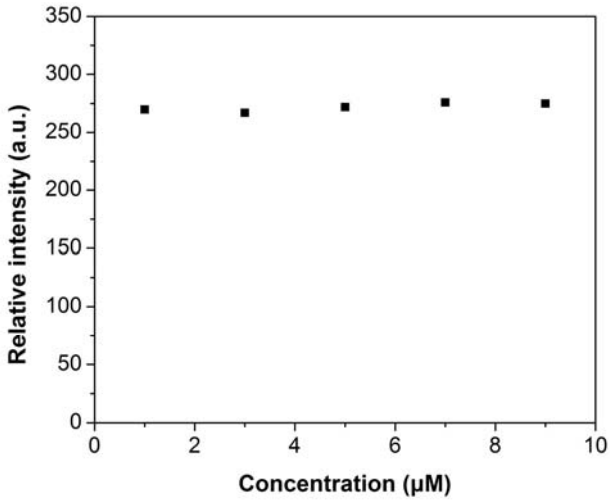

Fig. S14 Fluorescence titration of 2-AAQ with MA.

2.6 Molecular selectivity of SiO_2@MA-MIP nanoparticles

The fluorescence intensity of SiO_2@MA-MIP chemosensors showed a selective enhanceing effect by MA over other structural analogues including CA, MTD, ADP, DCH and BA. The difference could be due to the variation of size, steric shape and binding sites of the five analogues from the imprinted cavities. From the chemical structure (in left of Fig. S15), CA molecule possess almost identical molecular dimension with MA except the difference of the three substituents on the s-triazine ring. Although hydroxyl group in CA molecule can form hydrogen bond with 2-AAQ, the amount of hydrogen bond is fewer than that of MA when CA enters the imprinted cavity. So, this leads to lower enhancing effect. MTD and ADP are also analogous as MA except the difference of the amount of amino group on the s-triazine ring, resulting in lower enhancing effect. The steric shape of DCH has significant difference compared with that of MA and DCH is hard to diffuse into the imprinted cavities, leading to much low enhancing effect. BA is much smaller than MA and almost sterically unencumbered to enter into the imprinted cavity. Its fluorescence intensity is similar to DCH. Therefore, the lower enhancing effect of DCH and BA are mainly attributed to the nonspecific recognition, which also results in a very small difference of enhancing effects between imprinted and nonimprinted nanoparticles. In contrast, the SiO_2@MA-NIP nanoparticles have no selectivity to the six analogues (in right of Fig. S15).

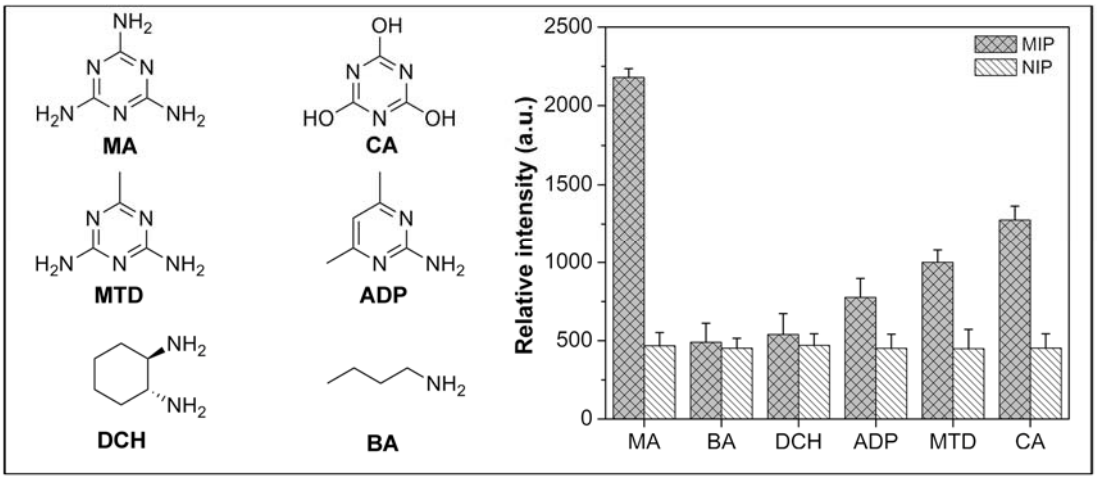

Fig. S15 Relative fluorescence intensity of SiO_2@MA-MIP and SiO_2@NIP to MA, CA, MTD, ADP, DCH

and BA, respectively.